Strong coupling between excitons in a two-dimensional atomic crystal and quasibound states in the continuum in a two-dimensional all-dielectric asymmetric metasurface

Peng Xie,[1,2,*] Zhengchen Liang,[1,3,*] Tongtong Jia,[1] Daimin Li,[1,2] Yixuan Chen,[1]
Peijie Chang,[1] Hong Zhang,[1,4] and Wei Wang[1,†]

[1]*College of Physics, Sichuan University, Chengdu 610064, China*
[2]*Institute of Atomic and Molecular Physics, Sichuan University, Chengdu 610065, China*
[3]*Department of Physics, Tsinghua University, Beijing 100084, China*
[4]*Key Laboratory of High Energy Density Physics and Technology of Ministry of Education, Sichuan University, Chengdu 610065, China*

(Received 28 January 2021; revised 12 September 2021; accepted 22 September 2021; published 30 September 2021)

We investigate the interaction between excitons in a two-dimensional atomic crystal and quasibound states in the continuum (q-BIC) in a two-dimensional all-dielectric asymmetric metasurface. By introducing coherent and incoherent coupling terms in a coupled oscillator model, we demonstrate the coexistence of coherent and incoherent coupling processes in the strongly coupled system and the resultant sub/superradiant polariton states. Based on the multipole decomposition method and near-field analysis of full wave simulations, we study the microscopic excitation of multipole components in q-BIC and their coupling to excitons. We reveal that not only the magnetic dipole but also the interference between electric dipole and its toroidal counterpart dominate in the exciton-BIC strong coupling regime. The fractions of the magnetic and electric dipole ingredients are modulated by the topology of the two-dimensional all-dielectric metasurface, exhibiting distinctly different features in the high- and low-energy hybrid modes in the strong coupling system. Our findings are expected to be of importance for both fundamental research in TMD-based light-matter interactions and practical applications in the design of novel, tunable exciton-polariton devices with high compactibility.

DOI: 10.1103/PhysRevB.104.125446

I. INTRODUCTION

Monolayers of transition-metal dichalcogenides (TMDs), as typical atomically thin two-dimensional (2D) direct-gap semiconductors, have attracted tremendous research interest in recent years due to their unique optical and electronic properties [1–3]. Excitons in monolayers of TMDs possess large oscillator strength, which is greatly favorable for studying strong light-matter interactions. In the strong coupling regime, the coupling strength between excitons and photons exceeds their individual dissipation rates and periodic coherent energy exchange occurs with the formation of new hybrid eigenstates that inherit both light (photonic) and matter (excitonic) characteristics. Such hybrid quasiparticles, known as exciton polaritons, possess many fascinating fundamental properties such as Bose condensation and superfluidity and [4,5] are finding use in a growing range of applications such as single photon transistors [6,7], all-optical switches [8,9], and polariton nanolasers [10].

Extensive studies have demonstrated strong coupling between monolayers of TMDs and various nanostructures, including photonic microcavities [11–13] and plasmonic nanoresonators such as periodic metallic nanocrystals [14,15] and nanocavities formed by single nanoparticles [16–19]. With their ability to confine light at the nanoscale with subwavelength-mode volume, strong coupling between excitons and photonic/plasmonic excitations can be easily realized in these hybrid systems. However, high-quality photonic resonators and efficient TMD-based light-matter coupling generally require both sophisticated fabrication techniques and appropriately locating the monolayer to overlap the strong field position inside the resonators, while the plasmonic nanostructures suffer from strong intrinsic dissipation due to Ohmic loss. Moreover, strong coherent coupling strength also requires complicated structure design to generate ultrasmall mode volumes, which brings inevitable challenges to both practical fabrication and compatibility.

Recently, all-dielectric photonic crystals or metasurfaces supporting optical bound states in the continuum (BICs) are emerging as a promising platform for the study of TMD-based exciton-photon interactions [20,21]. BICs, first introduced in quantum mechanics almost a century ago, are unusual localized dark states with energies embedded in the continuous spectrum of radiating waves, thus exhibiting infinitely small spectral width [22]. Only in the past decade has their rich physics been employed to engineer sharp resonances (high Q factors) in the form of quasi-BICs (q-BIC) in a variety of dielectric photonic systems [23–25]. Currently, q-BICs in all-dielectric photonic crystals or metasurfaces have been shown to be advantageous for enhanced light-matter coupling in the following aspects: (i) q-BICs provide an efficient light-trapping mechanism at resonances with very low optical losses determined only by radiation leakage [26–28], (ii) the radiative losses, or the Q factor of q-BICs can be readily engineered by controlling the configuration (shape, size, asymmetry, etc.) of the unit cell of the dielectric meta-atoms, and, importantly, (iii) the occurrence of q-BICs in

*These authors contributed equally to this work.
†w.wang@scu.edu.cn

all-dielectric systems generally associates with the simultaneous excitations of different optical resonances including electric, magnetic, and even the unusual toroidal modes [29]. Both the far-field radiation and the local field confinement at BIC resonances are governed by the mode constituents and the interplay between them, which can be readily controlled by engineering the configuration of dielectric meta-atoms to realize enhanced light-matter interactions and tailor the properties of matter [30].

Very recently, enhanced interaction of TMD monolayers with q-BICs has been observed in a 2D silicon metasurface with a greatly boosted second-harmonic generation of WS_2 excitons [21]. Strong coupling between TMD excitons and optical q-BICs in one-dimensional (1D) photonic crystal slabs (PCSs) has been theoretically reported to demonstrate an effective approach to engineering the exciton-polariton property by controlling the excitonic fraction in the polaritons [31]. Pronounced nonlinear polariton effects have also been experimentally demonstrated by strongly coupling a TMD monolayer to optical q-BICs in a 1D PCS [20]. However, extending strong TMD-BIC coupling to 2D dielectric metasurfaces is highly desired. The extra degrees of freedom in 2D metasurfaces would allow advanced dispersion engineering, providing a new opportunity to merge the BIC-inspired exciton polaritons with novel photonic designs. Moreover, 2D metasurfaces tend to support different types of modes that may contribute to q-BIC resonances, which would allow more convenient engineering of the mode constituents in q-BICs by tuning the 2D meta-atoms. This would provide rich physics for the hybrid polaritons in strong coupling regime. So far, strong coupling between TMD excitons and optical q-BICs in 2D metasurfaces, to the best of our knowledge, has not been reported. Particularly, the coupling mechanism between TMD excitons and different components in q-BICs and the resultant influence on the hybrid polariton property remains unexplored.

In this paper, we propose a hybrid system containing a 2D all-dielectric metasurface supporting q-BIC and a TMD monolayer. Coherent and incoherent interactions between TMD excitons and the q-BIC mode are studied in detail. Importantly, we also study the microscopic excitation of multipole components in q-BIC and their coupling to excitons using multipole decompositions combined with near-field analysis based on full wave simulations. We demonstrate that the fraction distributions of different multipole components exhibit distinctly different features in lower-energy and higher-energy polariton states, which can be readily tailored by subwavelength-scale engineering of the 2D meta-atoms. The proposed BIC-based all-dielectric platform combined with a TMD monolayer shows flexible tunability in hybrid polariton components and far-field emission characteristics, thus paving the way toward exciton-polariton devices with high compactibility.

II. RESULTS AND DISCUSSION

A. The strong coupling system

The proposed strongly coupled system, as depicted in Fig. 1(a), consists of a monolayer of tungsten disulfide (WS_2)

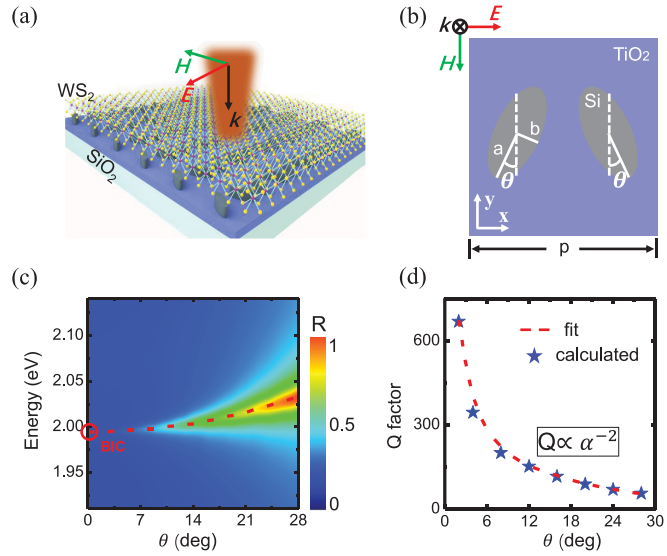

FIG. 1. (a) Three-dimensional schematic of the coupled system with a WS_2 monolayer on top of a square array of tilted silicon-bar pairs. (b) x-y plane view of the unit cell with array period $p = 400$ nm, ellipse semimajor axis $a = 100$ nm, and semiminor axis $b = 50$ nm. The height of the tilted silicon-bar pairs is 100 nm and the center-to-center distance between the bars is 200 nm. (c) Simulated reflectivity spectra as a function of θ (in color scale). The dashed red line and the solid red circle illustrate q-BIC dispersion and BIC, respectively. (d) The calculated (blue star points) and fitted (dashed red line) Q factors as a function of θ.

covering a 2D all-dielectric metasurface comprising an array of tilted silicon-bar pairs on top of a 140-nm-thick TiO_2 film, which is supported by a SiO_2 substrate. Under normal illumination, the bare 2D metasurface (in absence of the atop WS_2) with asymmetric pairs of tilted nanoparticles [32–35] can excite symmetry-protected BICs, a typical class of BICs originating from the spatial symmetry incompatibility between the bound state and the continuum [36]. Such all-dielectric metasurfaces can be fabricated using electron-beam lithography combined with reactive ion beam etching with high-precision control of the structural parameters [33,35]. A unique feature of symmetry-protected BICs is the occurrence of exceptionally ultrahigh-Q resonances. Importantly, slightly breaking in-plane symmetry of the 2D metasurface by engineering the asymmetric structural elements can obtain a direct transition from BICs to q-BICs with finite spectral width, thus offering an efficient approach to the control of Q factors and the resonance frequencies. In the present case, we define $\alpha = \sin\theta$ as the asymmetric parameter with θ representing the orientation of the long axis of the bar with respect to the y axis, as demonstrated in Fig. 1(b).

The BIC excitation and its change as a function of the asymmetry parameter can be readily simulated using the finite difference time domain (FDTD) method. In our simulation, a plane wave polarized in the x axis was employed to illuminate the square array of tilted silicon-bar pairs. Figure 1(c) gives the simulated reflectivity spectra of the bare metasurface as a function of tilted angle θ ranging from 0° to 28°. Two aspects can be clearly seen: (i) a symmetry-protected BIC (red circle) around 1.98 eV is excited with the characteristic of infinite

Q factor(i.e., no line width) for $\theta = 0^\circ$ and (ii) the resonance is blueshifted (red dashed line) and gradually broadened with finite Q factor as the tilted angle increases, corresponding to a clear transition from symmetry-protected BIC to q-BIC due to the break of the in-plane symmetry. Figure 1(d) gives the corresponding Q factors (blue stars) of the q-BIC modes as a function of θ by fitting the reflectivity spectra [Fig. 1(c)] to a Fano line shape. We find that the dependence of the Q factor on the asymmetry parameter follows $Q \propto 1/\alpha^2$, which is consistent with the typical inverse quadratic law for all designs of symmetry-broken meta-atoms [32].

B. Coherent and incoherent between excitons and q-BIC interactions

We now discuss the strong exciton-BIC coupling in the hybrid system. By tuning the asymmetry parameter α, we successfully brought q-BIC into resonance with the A excitons in the monolayer WS_2, which possess excitonic transition energy at (∼2.02 eV) at room temperature. To simulate the strongly coupled system, the dielectric function of the monolayer WS_2, for its optical response, was employed as a complex function of photon energy E with a sum of Lorentzian oscillators [37,38]:

$$\epsilon(E) = \epsilon_B + \sum_{j=1}^{N} \frac{f_j}{E_{0j}^2 - iE\gamma_j - E^2}. \tag{1}$$

Here, ϵ_B, f_j, E_{0j}, and γ_j are, respectively, the dielectric permittivity of the background, oscillator strengths, the resonance energies, and the damping rate of the jth order oscillator. Here, we applied the parameters reported in Refs. [14,37], in which five oscillators, i.e., $j = 5$, were used to present the optical response of the WS_2 monolayer with a careful fitting to the spectra measured on the WS_2 monolayer deposited on quartz. Of particular importance are the damping rates (γ_j) of excitons in single-layer WS_2, which play an important role in determining the coupling property in the hybrid system. A detailed discussion will be presented in later sections.

It is noted that the dielectric function of the WS_2 monolayer contains in-plane and out-of-plane components, which give slightly different in-plane and out-of-plane dielectric responses for different polarizations. In fact, we consider WS_2 monolayer as a 1-nm-thick isotropic dielectric film in our simulations. This is because an in-plane linearly polarized light was used to illuminate the whole structure at normal incidence with the electric field oscillating along the x direction, as shown in Fig 1(b). Therefore, the out-of-plane component of the dielectric material does not respond to the external excitation. If the sample is illuminated by a weak p-polarized light at oblique incidence, the electric field will have components in both x (in-plane) and z directions (out-of-plane); in this case, the effect of electric field on the material can also be generally neglected due to the fact that the out-of-plane response is expected to be rather weak due to the atomic thickness of WS_2 monolayer and low power excitations. The polarization dependency and the anisotropy of WS_2 monolayer could matter in the case of strong excitation under the illumination of intense light field, for example, ultrashort laser pulses.

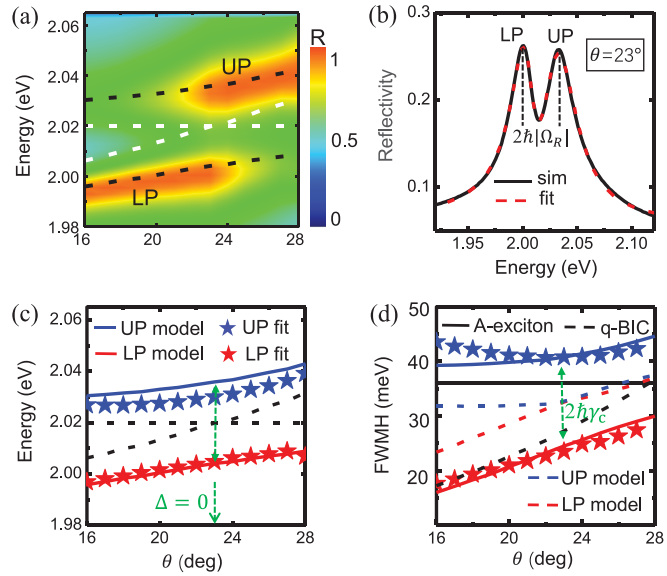

FIG. 2. (a) Reflectance spectra (in color scale) of the hybrid system as a function of θ overlapped with the uncoupled (dashed white lines) and coupled (dashed red lines) mode dispersions. (b) Fitted (dashed red) and simulated (solid black) reflectance spectrum of the hybrid system at zero detuning ($\theta = 23^\circ$). The dispersion relation (c) and spectral width (d) of the hybrid system obtained by a fitting (blue star points) and coupled oscillator model (solid line).

Figure 2(a) gives the 2D color map of the simulated reflectivity spectra as a function of the tilted angle θ ranging from 16° to 28°. A typical anticrossing behavior (dashed black lines) indicates the strong BIC-exciton coupling and the formation of hybrid (energetically) upper polariton (UP) and lower polariton (LP) modes.

To further explore the coupling property, we extracted the characteristics of the dispersions and spectral widths of the newly formed polariton modes by fitting the simulated reflectivity spectra to a Fano-shaped line shape, which results from the interference between nonresonant direct reflected light and the re-emitted resonant polariton modes, leading to an asymmetric Fano-shaped reflectivity spectrum $R(\omega) = |r(\omega)|^2$, with the reflectivity coefficient $r(\omega)$ given as [37]

$$r(\omega) = a_b + \sum_{j=\mathrm{UP,LP}} \frac{b_j \gamma_k e^{i\phi_j}}{\omega - \omega_j + i\gamma_j}. \tag{2}$$

Here, a_b, b_k, and ϕ_k are the background amplitude, amplitude, and spectral phase of the hybrid states, respectively. The dispersion and the reflectivity spectrum full width at half maximum (FWHM) of the hybrid UP and LP modes can be, respectively, characterized by ω_j and $2\gamma_j$. The fitted reflectivity spectra can very nicely reproduce the simulated results for all varying tilted angles (data are not shown here). Figure 2(b) plots the fitted spectrum at zero detuning, i.e., $\Delta = |\omega_{\mathrm{q-BIC}} - \omega_{\mathrm{X}}| = 0$ ($\theta = 23^\circ$), which gives an excellent match to the simulated results. A prominent normal mode splitting $\hbar\Omega_{\mathrm{NMS}}$ can therefore be estimated by roughly checking the peak-to-peak distance between the UP and LP resonant frequencies, which gives $\hbar\Omega_{\mathrm{NMS}} = 2\hbar|\Omega_R| \approx 34$ meV, with $\hbar\Omega_R$ defining the coherent coupling energy (or Rabi energy)

between the two subsystems. The extracted dispersion and FWHM of the hybrid states are given in Figs. 2(c) and 2(d) by blue and red star points, respectively. Clear anticrossing behavior in the dispersion lines indicates the occurrence of strong BIC-exciton coupling, where the normal mode splitting can be readily identified at zero detuning (green arrows). Interestingly, the polariton widths are strongly dependent on the asymmetry parameter and show a pronounced anticrossing behavior, leading to the UP/LP modes that are broader/narrower than the average width of the individual BIC and exciton modes. At zero detuning, The UP width exceeds that of the LP branch by over 10 meV.

The difference in polariton widths has been observed in many strongly coupled systems, including plasmonic nanocrystals coupled to organic semiconductors and single metallic nanoparticles coupled to a TMD monolayer [37,39,40]. The underlying mechanism has been extensively studied and explained as the coupling-induced sub- and superradiance originating from the incoherent damping process occurring via the continuum reservoir. We report here that sub- and superradiance also exist in the system of a BIC-based metasurface coupled to a TMD monolayer. To quantitatively evaluate the coherent and incoherent coupling properties, we employed the well-established coupled oscillator model (COM) and include both the coherent and incoherent coupling terms in a non-Hermitian Hamiltonian, which can be expressed as [41,42]

$$\hbar\left(\begin{bmatrix}\widetilde{\omega}_X & \Omega_R\\ \Omega_R^* & \widetilde{\omega}_B\end{bmatrix}-i\begin{bmatrix}0 & \gamma_c\\ \gamma_c & 0\end{bmatrix}\right)\begin{pmatrix}\alpha\\ \beta\end{pmatrix}=E\begin{pmatrix}\alpha\\ \beta\end{pmatrix}. \tag{3}$$

Here, $\widetilde{\omega}_{\mathrm{B}}=\omega_{\mathrm{B}}-i\gamma_{\mathrm{B}}$ and $\widetilde{\omega}_{\mathrm{X}}=\omega_{\mathrm{X}}-i\gamma_{\mathrm{X}}$ are, respectively, the q-BIC mode and the complex resonance frequencies of the uncoupled WS_2 excitonic mode. α and β are the Hopfield coefficients, which satisfy a relationship $|\alpha|^2+|\beta|^2=1$.

In this model, the excitonic transition energy of WS_2 is taken as $\hbar\omega_{\mathrm{X}}=2.02$ eV, while the corresponding population damping Γ_{X} is related to both radiative ($\Gamma_{\mathrm{X,rad}}$) and nonradiative ($\Gamma_{\mathrm{X,non-rad}}$) processes, leading to a total spectral width $\hbar\Gamma_{\mathrm{X,tot}}=\hbar\Gamma_{\mathrm{X}}=2\hbar\gamma_{\mathrm{X}}=\hbar\Gamma_{\mathrm{X,rad}}+\hbar\Gamma_{\mathrm{X,non-rad}}$. For high-quality WS_2 monolayers, spectroscopic measurements (reflectance, transmittance, absorptance, or photoluminescence) have revealed that the spectral linewidth *A*-exciton resonance is homogeneously broadened and dominated by the nonradiative damping with negligible inhomogeneous broadening and a pure dephasing process at room temperature [14]. Different values of spectral width $\hbar\Gamma_X$ can be obtained, depending on several factors such as the quality of the flake, the influence of the underlying substrates, and the experiment configuration of the static spectra acquisition [43–45]. In our simulation, we select a typical value of $\hbar\Gamma_X\approx 36$ meV with the contribution from the nonradiative process $\hbar\Gamma_{\mathrm{X,non-rad}}\approx 29$ meV and the radiative counterpart $\hbar\Gamma_{\mathrm{X,rad}}\approx 7$ meV, respectively.

For the q-BIC system, the angle-dependent dispersion $\hbar\omega_{\mathrm{B}}(\theta)$ [dashed line in Fig. 2(c)] and width $\hbar\Gamma_{\mathrm{B}}(\theta)=2\hbar\gamma_{\mathrm{B}}(\theta)$ [dashed black line in Fig. 2(d)] are extracted from the simulated reflectivity spectra for bare 2D metasurface in the absence of a WS_2 overlayer. In contrast to the WS_2 excitons, the spectral width of q-BIC is mainly governed by the radiative damping with negligible nonradiative damping due to the weak Ohmic loss in the all-dielectric medium.

With the above parameters, both the dispersion and the spectral width of the polariton states can be obtained by diagonalizing Eq. (3) with the optimal coherent coupling energy $\hbar|\Omega_R|=17$ meV and the cross damping term $\hbar\gamma_{\mathrm{c}}=4$ meV, as shown by the solid red and blue curves in Figs. 2(c) and 2(d). Apparently, the system is in the strong coupling regime since the coupling strength is large enough such that the criteria $\Omega_R>(\gamma_X+\gamma_B)/2$ is fulfilled. It is important to note that the simulated spectral widths can only be reproduced as long as a nonzero cross damping term is considered. We also plotted the calculated spectral widths for the case of $\hbar\gamma_{\mathrm{c}}=0$ meV. As shown in Fig. 2(d), the UP and LP widths as a function of tilted angle (dashed red and blue curves) exhibit a clear crossed profile, which is distinctly different from those for the case of $\hbar\gamma_{\mathrm{c}}=4$ meV (solid red and blue curves). This strongly indicates that two types of coupling processes coexist in the interaction between excitons in a WS_2 monolayer and q-BIC mode: (i) coherent coupling between two subsystems with the characteristics of coupling strength Ω_R and (ii) the incoherent damping pathway occurs as spontaneous photons from one subsystem to the vacuum continuum reservoir and then absorbed by another without any phase conservation, which eventually lead to the formation of sub/superradiant polariton states.

III. THE MULTIPOLAR EXPANSION OF Q-BIC STATE

In the above analysis, the TMD excitons and q-BIC excitation are considered as simple optical oscillators. Both the coherent and incoherent coupling process are included phenomenologically in COM, from which the dispersion and the spectral width of the hybrid states are evaluated. Essentially, COM has proven to be a powerful and efficient approach for evaluating the polariton energetics, the coupling strength, as well as the radiation characteristics of the hybrid modes. Successful application of COM has been reported in our previous work, where the polariton dispersion, as well as the coherent and incoherent coupling energy have been precisely obtained by COM in the system of plasmonic nanostructures coupling to organic semiconductors [39,41] or TMD monolayers [37,46]. The sub- and superradiant polariton dynamics predicted by COM have been confirmed by ultrafast time-resolved [40] pump-probe measurements [39,41].

However, in the system of 2D dielectric metasurface, the occurrence of q-BIC is generally accompanied by a simultaneous excitation of various electromagnetic modes, including electric dipole, magnetic dipole, and even their toroidal counterparts [29,47–49]. The fractions (or contributions) of different modes in q-BIC are very much dependent on the topological configuration of the metasurface. The coexistence of these multipole components and the interplay between them modulate the near-field response as well as the far-field radiation property, thus greatly influencing the polariton characteristics as they couple to TMD excitons in the hybrid system.

In this section, we aim to study in more detail the coupling of TMD excitons to different multipole components via a multipole decomposition technique to further explore the

coupling property and the resultant polariton features, including the fractions of individual modes in polariton states and their dependence on the asymmetry parameters, as well as the evolution of fractions with varying detuning under the effect of the interplay between different multipole modes.

A. Numerical calculation

In the present bare 2D metasurface in the absence of WS_2, the multipolar excitation features can be obtained by following the standard multipolar expansion on periodic nanostructures [29,48]:

$$
\begin{aligned}
P_\alpha &= \frac{1}{i\omega}\int d^3r\, j_\alpha,\\
M_\alpha &= \frac{1}{2c}\int d^3r(\vec{r}\times\vec{j})_\alpha,\\
T_\alpha &= \frac{1}{10c}\int d^3r[(\vec{r}\cdot\vec{j})r_\alpha - 2r^2 j_\alpha],\\
Q^{(e)}_{\alpha\beta} &= \frac{1}{2i\omega}\int d^3r\left[r_\alpha j_\beta + r_\beta j_\alpha - \frac{2}{3}\delta_{\alpha\beta}(\vec{r}\cdot\vec{j})\right],\\
Q^{(m)}_{\alpha\beta} &= \frac{1}{3c}\int d^3r[(\vec{r}\times\vec{j})_\alpha r_\beta + (\vec{r}\times\vec{j})_\beta r_\alpha],
\end{aligned}
\tag{4}
$$

with c being the constant speed of light, ω the driving frequency, n the refractive index, E_α the electric field, and $j_\alpha = -i\omega\epsilon_0(n^2-1)E_\alpha$ the current density under the Cartesian coordinate $\alpha, \beta = x, y, z$. The electric dipole P_α, the magnetic dipole M_α, the toroidal dipole T_α, the electric quadrupole $Q^{(e)}_{\alpha\beta}$, and the magnetic quadrupole $Q^{(m)}_{\alpha\beta}$ are referred to as multipolar modes P, M, T, Qe, and Qm, respectively. Indeed, there are various calculation methods for the multipolar expansion algorithm. Detailed discussions on the differences and connections among these methods have been summarized in Ref. [50]. In the present case, multipole decompositions of scattered waves are treated by writing the induced electric current density $j(r')$ as $\vec{j}(\vec{r'}) = \int_{V_s}\vec{j}(\vec{r})\delta(\vec{r'}-\vec{r})dr$ and then expending delta function $\delta(\vec{r'}-\vec{r})$ in a Taylor series around a point vector $\vec{r}_0$ located in the volume V_s. The main advantage of this approach is that the induced field can be expressed as the superposition of the field generated by the corresponding point multipole set regardless of the complexity of the charge and current distribution [51]. This method is not only widely used in periodic array structures [52–54] but also in single-particle nanostructures [55–57].

In our case, the calculation in Eqs. (4) is carried out by numerical integration in FDTD simulation. The all-dielectric nanostructure is modeled with periodic boundary conditions in the x and y directions, and with perfectly matched layer boundary conditions in the z direction. The FDTD simulation region, including the air, the silicon bars, and the TiO_2 substrate, forms a unit cell of the all-dielectric nanostructure, which represents the two features of the q-BIC mode: the symmetry breaking components (i.e., the silicon bars), and their spatial boundaries (i.e., the Si-TiO_2 interface). The numerical integrations in Eqs. (4) extend over the entire unit cell. The coordinate origin of $\vec{r}$ is at the origin point of the unit cell. In Fig. 3(a), we have extracted the current density $\vec{j}$ from the mesh grid. The result shows that the amplitude of $\vec{j}$ is mostly

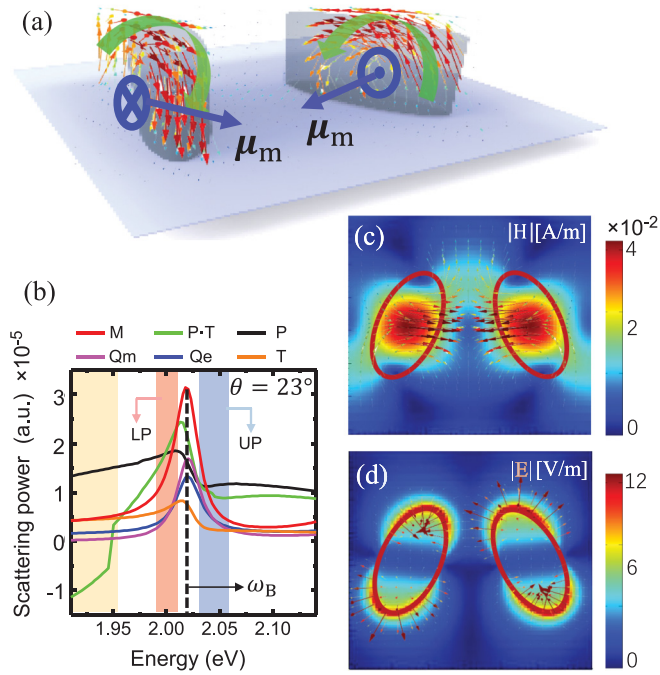

FIG. 3. (a) The displacement vector distribution in the square array of tilted silicon-bar pairs. (b) Scattering power of different multipole moments in the unit cell. Electric field (c) and magnetic field (d) distribution in x-y plane within each unit cell. The arrows denote the electric field and magnetic field vectors, respectively. All the above results are obtained at $\theta = 23°$.

focused on the two silicon bars, but orders of magnitude less in the substrates [the small blue arrows in Fig. 3(a)]. This is not beyond expectations, since that the q-BIC mode is originated from geometric symmetry breaking, which happens in our configuration, only in the silicon bars. The TiO_2 substrate which preserves the symmetry in the x-y plane but with a refractive index different from the silicon bars, serves as a spatial boundary for the q-BIC mode concentrating in the silicon bars. The spatial region of q-BIC near field in our system thus consists of the silicon bars plus the Si-TiO_2 interface.

The multipolar components derived from numerical calculation produce the scattering powers $I_P = (2\omega^4/3c^3)|\mathbf{P}|^2$, $I_M = (2\omega^4/3c^3)|\mathbf{M}|^2$, $I_T = (2\omega^6/3c^5)|\mathbf{T}|^2$, $I_{Qe} = (\omega^6/5c^5)|Q^{(e)}_{\alpha\beta}|^2$, and $I_{Qm} = (\omega^6/40c^5)|Q^{(m)}_{\alpha\beta}|^2$. Note that the multipolar expansion algorithm Eqs. (4) we applied here for the periodic nanostructures [48] is an approximated method of Ref. [58]; the only toroidal component considered here is T, a counterpart toroidal of P. The only interference term introduced is therefore between P and T:

$$
I_{P\text{-}T} = \frac{4\omega^5}{3c^4}(\mathbf{P}\cdot\mathbf{T}). \tag{5}
$$

B. Near-field characteristics

To give deep insight into the features of multipole components in the excitation of q-BIC, we first start with the near-field response at the q-BIC resonance obtained from FDTD simulations. Figure 3(a) demonstrates the distribution of current density $\vec{j}$ at the q-BIC resonance around 2.02 eV

for the case of tilted angle $\theta = 23^\circ$. We can clearly see intense current loops flowing oppositely around the two tilted silicon-bar pairs, leading to a strong magnetic response with magnetic dipole pointing normal to the long-axis plane (blue arrows). This strongly indicates that the contribution in q-BIC excitation is mainly from the magnetic dipole component, which can be readily confirmed by our multipole decomposition analysis. In Fig. 3(b), we plot the calculated scattering power of different multipolar components as a function of energy for $\theta = 23^\circ$. Apparently, the M mode exhibits a distinctly strong scattering peak at the q-BIC resonance ω_B with respect to that of others, which directly accounts for the strong magnetic response in the bar pairs [Fig. 3(a)]. Such a strong magnetic response can also be clearly seen in the simulated near-field distribution of the magnetic field at q-BIC resonance, as shown in Fig. 3(c).

In addition to the strong magnetic response, there also exists P and T modes offering relatively weak scattering power spectra with prominent Fano-like line shapes [black and orange curves in Fig. 3(b)]. This is in contrast to the M (red), Qe (blue), and Qm (purple) modes which show more or less Lorentzian line shapes with well-defined single peaks at the q-BIC resonance (dashed black line). We notice that the electric dipole mode shows rather weak scattering power at q-BIC resonance, which can be explained by the near-field distributions as shown Fig. 3(d). The corresponding electric field is mainly confined at the bar edges with the vectors (red arrows) pointing all over around the edges, and the maximum amplitude of the electric field is only up to 12 V/m. This field confinement is weaker than that in single-particle plasmonic nanostructures, in which the electric field is confined within a much smaller mode volume with maximum amplitude generally reaching several tens of volts per meter [18,19,40,46]. Spatial integration of the weak electric field with bad directionality over the bar pair finally gives weak scattering power.

Interestingly, it is also noted that the weak P mode strongly interacts with the other weak T mode, and their interaction gives different features at the low-energy and high-energy sides: the scattering power $I_{P\text{-}T}$, as a consequence of the inner product of mode vector **P** and **T**, gives very small or even negative values at energies lower than 1.95 eV (yellow region), which can be understood as a destructive interference between these two modes due to their vectors being orientated nearly perpendicular to each other. The scattering power then increases and finally reaches a considerably large positive value as the energy approaches ω_B. This indicates that the orientations of the P and T modes are almost parallel to each other since the scattering power exhibits $I_{P\text{-}T} \lesssim I_P + I_T$. A strong constructive interference between these two modes results in a considerable contribution to the far-field radiation at q-BIC resonance [green curve in Fig. 3(b)].

IV. MODULATION ON FRACTIONS IN POLARITON STATES

With the knowledge of multipolar origin of the q-BIC mode, we now look into the coupling of each multipole component with TMD excitons in more detail to explore the fraction distributions of each multipole components in polariton modes and the modulation effects on the fractions by the asymmetry parameter.

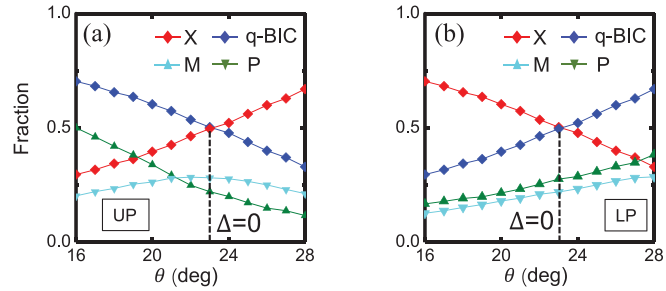

FIG. 4. The fractions of excitons (red) and q-BIC mode (blue) as a function of θ in (a) higher-energy UP and (b) lower-energy LP branch. The fractions of M (cyan) and P (green) mode are dominated in the q-BIC branch.

Utilizing the technique of multipole decompositions, one can not only obtain the varying fractions from the two strongly coupled collective modes [37] but also from each multipole component in q-BIC by the following [48]:

$$I_{scat} = I_P + I_T + I_{P\text{-}T} + I_M + I_{Qe} + I_{Qm} + O\left(\frac{1}{c^5}\right). \quad (6)$$

Assuming the small term $O(\frac{1}{c^5})$ from higher expansion that can be neglected, the strong coupling between the collective q-BIC excitations and the WS_2 excitons can be branched into the strong couplings between each multipolar mode (P, M, T, Qe, Qm) and the exciton mode, including the coupling between multipole modes P and T characterized by the interference term $I_{P\text{-}T}$. Specifically, the fraction of each multipolar component in the q-BIC mode strongly coupled to the WS_2 *A* exciton is extracted by (i) obtaining the fractions of q-BIC of UP/LP hybrid modes from COM optimized to our strong coupling system and (ii) determining the fractions of multipolar components P, M, T, Qe, and Qm in q-BIC of UP/LP by integrating the multipole moments over the unit cell at UP/LP resonances, respectively, as their weights. For our case, considering the small coefficient $2\omega^4/(3c^3)$ in the single-mode scattering power, the P and M components have dominating fractions in q-BIC, while the other three multipole modes (T, Qe, Qm) possess fraction proportion that are 10^{-14} order of magnitude smaller than that of P and M modes, which can be neglected.

In Fig. 4, we demonstrate the fractions of *A*-exciton and expanded multipole (P and M) modes as a function of the tilted angle in the UP branch (a) and the LP branch (b), respectively. For the UP state in Fig. 4(a), the fractions of the exciton (red) and q-BIC (blue) show two monotonous increasing/decreasing branches crossing at zero detuning ($\Delta = 0$), indicating that the hybrid state contains 50% exciton and 50% q-BIC fractions, which gives equal probabilities of finding the system in the exciton and q-BIC state, respectively. The fraction branches for the multipole M and P modes, however, cross at a smaller tilted angle of $\theta = 21^\circ$, with the P branch (green) monotonously decreasing and the M branch (cyan) slowly going up and then decreasing as θ becomes larger, leading to a maximum fraction occurring around zero detuning (dashed black line), while for the low energy LP

branch, the fractions for both M (cyan) and P (blue) mode grow monotonously with increasing θ, which is quite different from that for UP branch, as shown in Fig. 4(b)

To understand the behavior of the fraction distributions in the polariton states, we look back into the multipolar expansion spectra plotted in Fig. 3(b). The most significant difference between the UP and LP branches are the resonant frequencies. As shown in Fig. 3(b), the low-energy LP resonances lie in 1.99 eV $\sim$ 2.01 eV (red region), which are smaller than the q-BIC resonance ω_B at zero detuning (dashed black line). The high-energy UP processes resonant frequencies that are higher than ω_B, covering the energy band from 2.03 eV to 2.05 eV (blue region). Within the LP and UP frequency range, tuning the asymmetry parameter θ from 16° to 28° only affects the peak positions of each multipole component in the scattering power without changing their profiles, i.e., the distribution features for each component does not change as a function of θ.

Based on this fact, we first focus on the UP branch. It is noticed that, unlike the M mode exhibiting a single symmetric peak, the scattering power spectra of the P mode always exhibit a Fano-like increase-to-decrease line shape for the energies lower/higher than the WS_2 *A*-exciton resonance 2.02 eV ($\Delta = 0$), implying that its fraction is lowered down at energies higher than 2.02 eV, which includes the driving energy for UP resonance but not for LP resonance.

It is also noted that not all fractions of magnetic dipoles couple to WS_2 *A* excitons since the reflectance spectrum in Fig. 2(a) implies that some of the excitons are coupling with the subdominant electric dipoles. A suppression of the electric dipole fraction leads to a larger fraction of magnetic dipoles to couple with the exciton mode. Therefore, when the energy increases from the cross point (zero detuning) to the UP resonance, the fraction of the M mode coupling with excitons keeps lowering down, but a more steep suppression of the electric dipole fraction frees more uncoupled excitons for the dominant magnetic dipoles to couple with, thus compensating the fraction loss and making a slow peak for the magnetic dipole fraction in the UP branch.

On the contrary, for the LP branch, although the LP resonances are close to the peak position of Fano-like line shapes of electric dipole scattering power spectra, no asymmetric suppression of magnetic dipole fraction occurs since the magnetic dipole scattering spectra are single and almost symmetric peaks at 2.02 eV, which releases less exciton for the subdominant electric dipoles to couple with. Therefore, the normal trend of P and M mode fractions is preserved in the LP hybrid mode.

Essentially, the electric and magnetic near fields, as well as the multipolar mode fractions in the strong coupling can all be modulated by the multipolar features of q-BIC at the coupling cross point. Practically, the interference between multipole modes P and T, which has already been included in the current density information, leads to different line shapes in the scattering spectra. In our case, the M mode is engineered to perform a single and symmetric peak at zero detuning by controlling the structure parameters of tilted silicon-bar pairs in the full dielectric structure, and the subdominant P mode exhibits a Fano-like line shape with a peak at low energy and a dip at high energy in the scattering power spectrum. These two features help modulate the characteristics of the electric and magnetic, as well as the near-field property and mode fractions in the strongly coupled system between q-BIC and WS_2 *A*-exciton modes.

V. CONCLUSIONS

In summary, we proposed a hybrid system containing a 2D all-dielectric metasurface supporting q-BIC and a TMD monolayer. We investigate the interaction between TMD excitons and the q-BIC mode in the strong coupling regime. We demonstrated that two interaction processes (coherent and incoherent coupling) coexist in the strongly coupled system and lead to the formation of sub/superradiant polariton states. We also studied the microscopic excitation of multipole components in q-BIC and their coupling to excitons using multipole decompositions combined with near-field analysis based on full wave simulations. We reveal that the magnetic and electric dipole mode dominate in the strong exciton-BIC coupling. The fraction distributions of the M and P modes behave completely differently in UP and LP states, which is mainly controlled by the fraction of the electric dipole mode in the q-BIC state. The fraction distributions of each mulitpole component in the hybrid states can be readily tailored by subwavelength-scale engineering of the 2D meta-atoms, which may pave the way toward novel, tunable exciton-polariton devices with high compactibility.

ACKNOWLEDGMENTS

This work is supported by the National Natural Science Foundation of China (Grants No. 11974254 and No. 11974253), the National Key R&D Program of China (No. 2017YFA0303600), Science Speciality Program of Sichuan University (Grant No. 2020SCUNL210) and the Innovation Program of Sichuan University (Grant No. 2018SCUH0074).

[1] G. R. Bhimanapati, Z. Lin, V. Meunier, Y. Jung, J. Cha, S. Das, D. Xiao, Y. Son, M. S. Strano, V. R. Cooper, L. B. Liang, S. G. Louie, E. Ringe, W. Zhou, S. S. Kim, R. R. Naik, B. G. Sumpter, H. Terrones, F. N. Xia, Y. L. Wang, J. Zhu, D. Akinwande, N. Alem, J. A. Schuller, R. E. Schaak, M. Terrones, and J. A. Robinson, ACS Nano **9**, 11509 (2015).

[2] S. Manzeli, D. Ovchinnikov, D. Pasquier, O. V. Yazyev, and A. Kis, Nat. Rev. Mater. **2**, 17033 (2017).

[3] G. Wang, A. Chernikov, M. M. Glazov, T. F. Heinz, X. Marie, T. Amand, and B. Urbaszek, Rev. Mod. Phys. **90**, 021001 (2018).

[4] J. Kasprzak, M. Richard, S. Kundermann, A. Baas, P. Jeambrun, J. M. J. Keeling, F. M. Marchetti, M. H. Szymanska, R. Andre, J. L. Staehli, V. Savona, P. B. Littlewood, B. Deveaud, and L. S. Dang, Nature (London) **443**, 409 (2006).

[5] A. Amo, J. Lefrere, S. Pigeon, C. Adrados, C. Ciuti, I. Carusotto, R. Houdre, E. Giacobino, and A. Bramati, Nat. Phys. **5**, 805 (2009).

[6] D. E. Chang, A. S. Sorensen, E. A. Demler, and M. D. Lukin, Nat. Phys. **3**, 807 (2007).

[7] D. E. Chang, V. Vuletic, and M. D. Lukin, Nat. Photon. **8**, 685 (2014).

[8] K. F. MacDonald, Z. L. Samson, M. I. Stockman, and N. I. Zheludev, Nat. Photon. **3**, 55 (2009).

[9] P. Vasa, R. Pomraenke, G. Cirmi, E. De Re, W. Wang, S. Schwieger, D. Leipold, E. Runge, G. Cerullo, and C. Lienau, ACS Nano **4**, 7559 (2010).

[10] P. Bhattacharya, T. Frost, S. Deshpande, M. Z. Baten, A. Hazari, and A. Das, Phys. Rev. Lett. **112**, 236802 (2014).

[11] X. Z. Liu, T. Galfsky, Z. Sun, F. N. Xia, E. C. Lin, Y. H. Lee, S. Kena-Cohen, and V. M. Menon, Nat. Photon. **9**, 30 (2015).

[12] S. Dufferwiel, S. Schwarz, F. Withers, A. A. P. Trichet, F. Li, M. Sich, O. Del Pozo-Zamudio, C. Clark, A. Nalitov, D. D. Solnyshkov, G. Malpuech, K. S. Novoselov, J. M. Smith, M. S. Skolnick, D. N. Krizhanovskii, and A. I. Tartakovskii, Nat. Commun. **6**, 8579 (2015).

[13] M. Sidler, P. Back, O. Cotlet, A. Srivastava, T. Fink, M. Kroner, E. Demler, and A. Imamoglu, Nat. Phys. **13**, 255 (2017).

[14] S. Wang, S. Li, T. Chervy, A. Shalabney, S. Azzini, E. Orgiu, J. A. Hutchison, C. Genet, P. Samori, and T. W. Ebbesen, Nano Lett. **16**, 4368 (2016).

[15] W. Liu, B. Lee, C. H. Naylor, H.-S. Ee, J. Park, A. T. C. Johnson, and R. Agarwal, Nano Lett. **16**, 1262 (2016).

[16] S. Lepeshov, M. Wang, A. Krasnok, O. Kotov, T. Zhang, H. Liu, T. Jiang, B. Korgel, M. Terrones, Y. Zheng, and A. Alu, ACS Appl. Mater. Inter. **10**, 16690 (2018).

[17] J. Cuadra, D. G. Baranov, M. Wersall, R. Verre, T. J. Antosiewicz, and T. Shegai, Nano Lett. **18**, 1777 (2018).

[18] J. Wen, H. Wang, W. Wang, Z. Deng, C. Zhuang, Y. Zhang, F. Liu, J. She, J. Chen, H. Chen, S. Deng, and N. Xu, Nano Lett. **17**, 4689 (2017).

[19] D. Zheng, S. Zhang, Q. Deng, M. Kang, P. Nordlander, and H. Xu, Nano Lett. **17**, 3809 (2017).

[20] V. Kravtsov, E. Khestanova, F. A. Benimetskiy, T. Ivanova, A. K. Samusev, I. S. Sinev, D. Pidgayko, A. M. Mozharov, I. S. Mukhin, M. S. Lozhkin, Y. V. Kapitonov, A. S. Brichkin, V. D. Kulakovskii, I. A. Shelykh, A. I. Tartakovskii, P. M. Walker, M. S. Skolnick, D. N. Krizhanovskii, and I. V. Iorsh, Light: Sci. Appl. **9**, 56 (2020).

[21] N. Bernhardt, K. Koshelev, S. J. U. White, K. W. C. Meng, J. E. Froch, S. Kim, T. Toan Trong, D.-Y. Choi, Y. Kivshar, and A. S. Solntsev, Nano Lett. **20**, 5309 (2020).

[22] K. Koshelev, A. Bogdanov, and Y. Kivshar, Sci. Bull. **64**, 836 (2019).

[23] Z. Sadrieva, K. Frizyuk, M. Petrov, Y. Kivshar, and A. Bogdanov, Phys. Rev. B **100**, 115303 (2019).

[24] C. W. Hsu, B. Zhen, J. Lee, S.-L. Chua, S. G. Johnson, J. D. Joannopoulos, and M. Soljacic, Nature (London) **499**, 188 (2013).

[25] H. M. Doeleman, F. Monticone, W. den Hollander, A. Alu, and A. F. Koenderink, Nat. Photon. **12**, 397 (2018).

[26] D. Lin, P. Fan, E. Hasman, and M. L. Brongersma, Science **345**, 298 (2014).

[27] S. Kruk and Y. Kivshar, ACS Photon. **4**, 2638 (2017).

[28] E. Tiguntseva, K. Koshelev, A. Furasova, P. Tonkaev, V. Mikhailovskii, E. V. Ushakova, D. G. Baranov, T. Shegai, A. A. Zakhidov, Y. Kivshar, and S. V. Makarov, ACS Nano **14**, 8149 (2020).

[29] C. Zhou, S. Li, Y. Wang, and M. Zhan, Phys. Rev. B **100**, 195306 (2019).

[30] S. T. Ha, Y. H. Fu, N. K. Emani, Z. Pan, R. M. Bakker, R. Paniagua-Dominguez, and A. I. Kuznetsov, Nat. Nanotechnol. **13**, 1042 (2018).

[31] K. L. Koshelev, S. K. Sychev, Z. F. Sadrieva, A. A. Bogdanov, and I. V. Iorsh, Phys. Rev. B **98**, 161113(R) (2018).

[32] K. Koshelev, S. Lepeshov, M. K. Liu, A. Bogdanov, and Y. Kivshar, Phys. Rev. Lett. **121**, 193903 (2018).

[33] A. Tittl, A. Leitis, M. Liu, F. Yesilkoy, D.-Y. Choi, D. N. Neshev, Y. S. Kivshar, and H. Altug, Science **360**, 1105 (2018).

[34] M. Liu, D. A. Powell, R. Guo, I. V. Shadrivov, and Y. S. Kivshar, Adv. Opt. Mater. **5**, 1600760 (2017).

[35] F. Yesilkoy, E. R. Arvelo, Y. Jahani, M. Liu, A. Tittl, V. Cevher, Y. Kivshar, and H. Altug, Nat. Photon. **13**, 390 (2019).

[36] C. W. Hsu, B. Zhen, A. D. Stone, J. D. Joannopoulos, and M. Soljacic, Nat. Rev. Mater. **1**, 16048 (2016).

[37] S. Zhang, H. Zhang, T. Xu, W. Wang, Y. Zhu, D. Li, Z. Zhang, J. Yi, and W. Wang, Phys. Rev. B **97**, 235401 (2018).

[38] Y. L. Li, A. Chernikov, X. Zhang, A. Rigosi, H. M. Hill, A. M. van der Zande, D. A. Chenet, E. M. Shih, J. Hone, and T. F. Heinz, Phys. Rev. B **90**, 205422 (2014).

[39] W. Wang, P. Vasa, R. Pomraenke, R. Vogelgesang, A. De Sio, E. Sommer, M. Maiuri, C. Manzoni, G. Cerullo, and C. Lienau, ACS Nano **8**, 1056 (2014).

[40] P. Xie, Z. Liang, Z. Li, W. Wang, W. Wang, T. Xu, X. Kuang, L. Qing, D. Li, and J. Yi, Phys. Rev. B **101**, 045403 (2020).

[41] P. Vasa, W. Wang, R. Pomraenke, M. Lammers, M. Maiuri, C. Manzoni, G. Cerullo, and C. Lienau, Nat. Photon. **7**, 128 (2013).

[42] C. Ropers, D. J. Park, G. Stibenz, G. Steinmeyer, J. Kim, D. S. Kim, and C. Lienau, Phys. Rev. Lett. **94**, 113901 (2005).

[43] S. Wang, Q. Le-Van, F. Vaianella, B. Maes, S. Eizagirre Barker, R. H. Godiksen, A. G. Curto, and J. Gomez Rivas, ACS Photon. **6**, 286 (2019).

[44] X. Han, K. Wang, X. Xing, M. Wang, and P. Lu, ACS Photon. **5**, 3970 (2018).

[45] M. Wang, A. Krasnok, T. Zhang, L. Scarabelli, H. Liu, Z. Wu, L. M. Liz-Marzan, M. Terrones, A. Alu, and Y. Zheng, Adv. Mater. **30**, 1705779 (2018).

[46] P. Xie, D. Li, Y. Chen, P. Chang, H. Zhang, J. Yi, and W. Wang, Phys. Rev. B **102**, 115430 (2020).

[47] W. X. Lim, S. Han, M. Gupta, K. F. MacDonald, and R. Singh, Appl. Phys. Lett. **111**, 061104 (2017).

[48] P. C. Wu, C. Y. Liao, V. Savinov, T. L. Chung, W. T. Chen, Y. W. Huang, P. R. Wu, Y. H. Chen, A. Q. Liu, N. I. Zheludev, and D. P. Tsai, ACS Nano **12**, 1920 (2018).

[49] S. Y. Li, C. B. Zhou, T. T. Liu, and S. Y. Xiao, Phys. Rev. A **100**, 063803 (2019).

[50] A. B. Evlyukhin and B. N. Chichkov, Phys. Rev. B **100**, 125415 (2019).

[51] P. Grahn, A. Shevchenko, and M. Kaivola, New J. Phys. **14**, 093033 (2012).

[52] N. Papasimakis, V. A. Fedotov, K. Marinov, and N. I. Zheludev, Phys. Rev. Lett. **103**, 093901 (2009).

[53] T. Kaelberer, V. A. Fedotov, N. Papasimakis, D. P. Tsai, and N. I. Zheludev, Science **330**, 1510 (2010).

[54] E. Takou, A. C. Tasolamprou, O. Tsilipakos, Z. Viskadourakis, M. Kafesaki, G. Kenanakis, and E. N. Economou, Phys. Rev. Appl. **15**, 014043 (2021).

[55] X. L. Zhang, S. B. Wang, Z. F. Lin, H. B. Sun, and C. T. Chan, Phys. Rev. A **92**, 043804 (2015).

[56] A. E. Miroshnichenko, A. B. Evlyukhin, Y. F. Yu, R. M. Bakker, A. Chipouline, A. I. Kuznetsov, B. Luk'yanchuk, B. N. Chichkov, and Y. S. Kivshar, Nat. Commun. **6**, 8069 (2015).

[57] J. A. Parker, H. Sugimoto, B. Coe, D. Eggena, M. Fujii, N. F. Scherer, S. K. Gray, and U. Manna, Phys. Rev. Lett. **124**, 097402 (2020).

[58] E. A. Gurvitz, K. S. Ladutenko, P. A. Dergachev, A. B. Evlyukhin, A. E. Miroshnichenko, and A. S. Shalin, Laser Photonics Rev. **13**, 1800266 (2019).